The Astronomical Journal, 159:106 (14pp), 2020 March https://doi.org/10.3847/1538-3881/ab66b4

A Search for Transiting Planets in the Globular Cluster M4 with *K2*: Candidates and Occurrence Limits

Joshua J. Wallace, Joel D. Hartman, and Gáspár Á. Bakos[1]
Department of Astrophysical Sciences, Princeton University, 4 Ivy Lane, Princeton, NJ 08544, USA; joshuawallace800@gmail.com
Received 2019 September 20; revised 2019 December 7; accepted 2019 December 30; published 2020 February 13

Abstract

We perform a search for transiting planets in the NASA *K2* observations of the globular cluster (GC) M4. This search is sensitive to larger orbital periods ($P \lesssim 35$ days, compared to the previous best of $P \lesssim 16$ days), and at the shortest periods, smaller planet radii ($R_p \gtrsim 0.3\,R_J$, compared to the previous best of $R_p \gtrsim 0.8\,R_J$) than any previous search for GC planets. Seven planet candidates are presented. An analysis of the systematic noise in our data shows that most, if not all, of these candidates are likely false alarms. We calculate planet occurrence rates assuming our highest significance candidate is a planet and occurrence rate upper limits assuming no detections. We calculate 3σ occurrence rate upper limits of 6.1% for 0.71–2 R_J planets with 1–36 days periods and 16% for 0.36–0.71 R_J planets with 1–10 days periods. The occurrence rates from *Kepler*, *TESS*, and radial velocity studies of field stars are consistent with both a nondetection of a planet and detection of a single hot Jupiter in our data. Comparing to previous studies of GCs, we are unable to place a more stringent constraint than Gilliland et al. for the radius–period range they were sensitive to, but do place tighter constraints than both Weldrake et al. and Nascimbeni et al. for the large-radius regimes to which they were sensitive.

Unified Astronomy Thesaurus concepts: Exoplanets (498); Globular star clusters (656); Hot Jupiters (753); Transit photometry (1709)

1. Introduction

The globular cluster (GC) M4 (NGC 6121) was observed by the *K2* mission (Howell et al. 2014) during its Campaign 2. These data underwent a blanket search for variable objects in our previous work (Wallace et al. 2019a), but did not receive a focused search for planetary transits. Any constraints that could be put on planet occurrence rates in a GC would be of scientific interest. GCs provide more-or-less homogeneous populations of metal-poor stars: M4, in particular, has a metallicity of [Fe/H] ≈ -1.2 (Harris 1996, 2010 edition). As such, they would provide valuable test beds for theories about planet formation and its dependence on stellar metallicities (e.g., Ida & Lin 2004; Johansen et al. 2009; Ercolano & Clarke 2010; Johnson et al. 2010; Johnson & Li 2012), assuming such formation mechanisms also take into account the denser stellar environment. These high stellar densities could also provide a fruitful testbed for dynamical planet formation and evolution theories. The relatively large number of stellar encounters in GCs, due to both their old ages and high stellar densities, are thought to kick planets out of planetary systems, especially those on wide orbits (Sigurdsson 1992; Bonnell et al. 2001; Davies & Sigurdsson 2001; Fregeau et al. 2006; Spurzem et al. 2009). However, stellar encounters are also expected to increase the probability of formation of hot Jupiters (HJs) via high-eccentricity migration in some cases (Hamers & Tremaine 2017). For reference, for this work, a typical definition of an HJ is a planet with a radius $\gtrsim 0.8 R_J$ and an orbital period $\lesssim 10$ days. An enhanced HJ occurrence rate in GCs may suggest a preference for dynamical formation pathways in our own neighborhood for close-in planets. And finally, HJs are expected to undergo tidal orbital decay on Gyr timescales (e.g., Penev et al. 2018), and the old ages of GCs may be helpful in testing this theoretical expectation.

M4 holds the distinction of possessing the only planet known in a GC, PSR 1620-26 b, a planetary-mass object orbiting a pulsar–white dwarf binary (Backer et al. 1993; Thorsett et al. 1993, 1999; Michel 1994; Rasio 1994; Arzoumanian et al. 1996; Ford et al. 2000; Richer et al. 2003), with its mass measured by Sigurdsson et al. (2003) to be $2.5 \pm 1\,M_J$. Work since its discovery has shown that this planet may have formed later in the cluster's life, rather than from a protostellar disk. For example, Beer et al. (2004) propose a model where a stellar encounter during the common envelope phase that led to the formation of the pulsar caused a dynamical instability in the dense equatorial wind formed as part of the common envelope phase. As such, PSR 1620-26 b may not be able to provide constraints on planet formation processes in GCs that are contemporaneous with star formation.

Given the relatively large distance to M4 of 1.8 kpc (Hendricks et al. 2012; Kaluzny et al. 2013; Braga et al. 2015; Neeley et al. 2015), a wide-scale radial velocity (RV) survey to search for planets is impractical, but a photometric survey to search for transits is feasible. Despite its distance, M4 is nevertheless the closest GC, and it has a relatively sparse core, so it is perhaps the best target for discovering additional GC planets.

Previous searches for transiting planets have been made in GCs. The largest to date are the *Hubble Space Telescope* (*HST*) campaign of Gilliland et al. (2000) and the ground-based campaign of Weldrake et al. (2005), both searching for planetary transits in 47 Tuc. Gilliland et al. (2000) state that the reason for choosing this cluster (its distance is about twice that of M4) is because its spatial and main-sequence brightness distributions matched well the capabilities of *HST*. They obtained high-precision photometry for ~34,000 stars over an observing campaign of 8.3 days. With the then-current understanding of HJ occurrence rates, they had expected to find ~17 planets; however, they found none. More recently,

[1] MTA Distinguished Guest Fellow, Konkoly Observatory.

Masuda & Winn (2017) revised the expected number of planets that Gilliland et al. would have found to $2.2^{+1.6}_{-1.1}$, based on an updated understanding of planet occurrence from the *Kepler* mission. This revised number additionally does not account for the lower metallicity of 47 Tuc ([Fe/H] ≈ -0.7; McWilliam & Bernstein 2008) relative to the *Kepler* stars, which are primarily field stars. This is expected to revise the number even lower due to the metallicity dependence of the occurrence rate of HJs (Santos et al. 2001; Fischer & Valenti 2005; Petigura et al. 2018). Weldrake et al. (2005) used the Australian National University 40 inch telescope at Siding Spring observatory over 33 nights and obtained a much wider field of view than Gilliland et al.'s *HST* observations, observing out to 60% of 47 Tuc's tidal radius. They obtained light curves for ∼110,000 stars (though only ∼20,000 of these had sufficiently low scatter to be sensitive to HJs) and could detect giant planets with periods up to 16 days. Their calculated expected planet yield was ∼7 planets (based on 1 R_J planets with periods less than 16 days and an intrinsic formation rate of 0.8%), but they found none. Masuda & Winn (2017) revised the expected number of planets from this survey down by about a factor of four. Both the Gilliland et al. (2000) and Weldrake et al. (2005) surveys were not sensitive to much other than HJs. Other searches for transiting exoplanets in GCs include: the search of Weldrake et al. (2008) in ω Cen, which for the most part was sensitive only to planets with radii $>1.5R_J$ and had no detections; and Nascimbeni et al. (2012) in NGC 6397, which with a null detection and ∼5000 light curves, were not able to derive constraints on planet occurrence that fell below the occurrence rates measured by *Kepler*.

M4 was in the field of view of the *Kepler* telescope during Campaign 2 (running from 2014 August 23 to November 10) of the *K2* mission, and as mentioned, continuous observations of a portion of this cluster were included in the data downloaded from the telescope. Though the original proposals to obtain these data were focused on observing RR Lyrae variables in the cluster, the excellent photometry and long-term coverage of M4 allows for the detection of other variable objects, potentially including transiting HJs. The *Kepler* telescope and detector were not designed with GC observations in mind: the $\sim 4''$ pixel^{-1} image resolution leads to significant blending in the images, and the periodic telescope drift experienced during the *K2* mission produces systematic noise in the photometry.

Despite these problems, the longer observation span of *K2* Campaign 2, relative to the previous GC transiting planet searches, potentially opens a new regime of planetary orbital period to explore and to place constraints on GC planet occurrence. The longer observations also increase the number of observed transits for orbits of a given period relative to the previous surveys, helping to boost sensitivity to smaller-radius planets in the period ranges that have already been probed by other GC studies. Given the scientific motivation for finding planets in GCs and the new parameter space opened for exploration by these data, and because the reduced data have scientific utility in addition to permitting a transit search (see our variable catalog in Wallace et al. 2019a), there is more than sufficient merit to motivate the effort for the search. We summarize our photometric reductions and explain our transit search methodology in Section 2, present the results of our transit search in Section 3, and provide planet occurrence rates and limits in Section 4. We then discuss the results in Section 5, and conclude in Section 6.

2. Method

2.1. Photometric Processing

Our photometric processing pipeline is fully described in Wallace et al. (2019a), and is similar to that of Soares-Furtado et al. (2017). We provide a brief summary here. M4 was observed by *K2* for ∼79 days in 2014, during the mission's Campaign 2. Given the high degree of blending in the images, we decided to use image subtraction (Alard & Lupton 1998) to extract light curves for the objects. The *Gaia* first data release (DR1) source catalog (Gaia Collaboration et al. 2016a, 2016b) was used as an astrometric and photometric reference catalog. We included all sources with $G < 19$. DR1 was used instead of the *Gaia* second data release (DR2) catalog, owing to our beginning this study prior to *Gaia* DR2. Using the DR1 catalog leads to slightly higher upper limits on planet occurrence than could have been derived with the additional sources in DR2; however, the improvement that could be expected from using DR2 is too small to justify the additional effort of redoing the photometric reduction. In using *Gaia* DR1 as a photometric reference catalog, we had to convert from G to our *Kepler* instrumental magnitudes. We found that a simple additive conversion was all that was needed, likely due to the similar bandpasses of the two instruments,with the conversion from instrumental magnitude M_I being $G = M_I + 25.275$ mag. Any error in the reference magnitudes would lead to errors in the measured transit depths, but not in the significance of any signals, as all of the light curve points would be affected equally.

The photometry was extracted for apertures of 1.5, 1.75, 2.0, 2.25, 2.5, 2.75, and 3.0 pixels in radius. At the end of our processing, we found which aperture radius minimized the photometric scatter as a function of G and used the data from the corresponding aperture for all objects of a given magnitude throughout our analysis. For reference, the typical full width at half maximum value for the point-spread function of the images was ∼1.5 pixels.

After extracting this raw photometry, systematic variability from the spacecraft roll was cleaned up based our implementation of the algorithm developed by Vanderburg & Johnson (2014) and Vanderburg et al. (2016). The light curves were then further cleaned of common systematic trends, using the trend filtering algorithm (TFA; Kovács et al. 2005) as implemented in `VARTOOLS` (Hartman & Bakos 2016). For each aperture, 250 light curves were selected from uniform bins of image position and magnitude to be the trend light curves for the TFA. The total number of light curves thus produced was 4554. In this work, all objects are referred to by the identifiers assigned them in Wallace et al. (2019a); see Table 1 in that work. All of the raw and processed light curves are available at Wallace et al. (2019b).[2]

2.2. Transit Search

All 4554 light curves were searched for planet transits using the `VARTOOLS` implementation of the box-fitting least squares

[2] Published at Princeton University's DataSpace and licensed under a Creative Commons Attribution 4.0 International License, accessible at http://arks.princeton.edu/ark:/88435/dsp01h415pd368.

(BLS; Kovács et al. 2002) algorithm. The light curves were sigma clipped prior to the search (5σ, three iterations). We ran some injected transits through our pipeline to ensure that they would be recoverable even with the photometric post-processing and sigma clipping. We searched periods between one day and the maximum observation length of the given light curves (most having the maximum length of ∼78 days, which is slightly shorter than the full span of observations, owing to our need to trim the first ∼1 day of data). A one-day orbit around the most massive and evolved cluster-member stars under consideration ($0.81\ M_{\odot}$) has an orbital semimajor axis of $3.9\ R_{\odot}$, compared to a stellar radius of $4.9\ R_{\odot}$ for these same stars. Thus, for the handful of the most evolved stars under consideration, one-day orbits are not possible—but they are possible for the vast majority of the stars we consider.

The range of values for the fractional transit duration q used in the search varied between $0.1 \times q_{\rm exp}$ and $2 \times q_{\rm exp}$, with $q_{\rm exp}$ being the expected transit duration at a given period based on the density of the given star (see the next two paragraphs), assuming a circular orbit and that the impact parameter b is zero. The minimum q searched was adjusted as necessary, so that it was never less than $(\Delta t)_{\rm min}/P$, with $(\Delta t)_{\rm min}$ being the minimum time between observations (the *Kepler* cadence, 29.4 minutes, adjusted slightly based on the actual BJD values of the observations) and P being the period being searched. The number of phase bins used was set to $2/q_{\rm min}$, with $q_{\rm min}$ here being $0.1 \times q_{\rm exp}$, up to a maximum value of 2100. This value is based on the expected transit duration of the shortest-period planets around the smallest-radius stars in our sample. With there being less than 4000 measurements per light curve, a greater number of phase bins would not have been useful anyway.

Stellar densities were calculated based on an isochrone fit for the cluster and the V magnitudes taken from Mochejska et al. (2002). This isochrone-based density determination produced incorrect densities for objects that were not cluster members—but given that they were not included in our final analysis, this did not matter. For objects not found in the Mochejska et al. (2002) catalog, their V magnitudes were converted from G based on a second-degree polynomial fit between G and the Mochejska et al. (2002) V magnitudes of the matched objects. The isochrone was taken from the calculations of Yi et al. (2001). For the isochrone, we assumed a metallicity of $[{\rm Fe/H}] = -1.2$ (Harris 1996, 2010 edition) and an estimated age of 11.3 Gyr based on our fit to the data. The V magnitudes were used instead of *Gaia* G because this calculation was performed earlier in *Gaia*'s mission and our isochrone database had not yet incorporated results that used the *Gaia* bandpass. The V magnitudes were converted to absolute magnitudes assuming a cluster distance of 1.8 kpc (Hendricks et al. 2012; Kaluzny et al. 2013; Braga et al. 2015; Neeley et al. 2015) and an A_V extinction of 1.24 mag based on our fit to the data, a value ∼0.15 less than the mean value found by Hendricks et al. (2012). We also note that there is differential reddening across the cluster, with Hendricks et al. (2012) finding the difference between the lowest and the highest $E(B-V)$ values to be ∼0.2 mag.

The use of stellar density in the BLS calculation tailors the transit duration range that is searched to those expected for a planet around a star of the given density. This boosts sensitivity to physically likely transit scenarios. This is in contrast to our previous search in Wallace et al. (2019a), which was not restricted to only transit durations consistent with planetery transits, and is part of the reason we were better able to find planet candidates in this search (the previous search found none). Given the fairly wide distribution in q that we search ($0.1 \times q_{\rm exp}$ to $2 \times q_{\rm exp}$), the search is insensitive to modest errors in density.

The phase-folded light curves and periodograms for the periods of the top five periodogram peaks were then examined by eye for significance. We used the `checkplot` module of `astrobase` (Bhatti et al. 2017) for this by-eye examination. As part of this, we excluded signals that were obviously not planet transits (e.g., RR Lyrae and eclipsing binaries, as well as objects blended with them). We also found that a large and temporary systematic variation in brightness occurred about halfway through the observation in the light curves of many of the objects, at the point in the campaign when the roll direction of the spacecraft changed. This light curve systematic in some cases phased up with other outliers to produce large-period BLS signals; cases where this happened were determined by eye and removed. In ambiguous cases, we erred on the side of completeness and included the objects in our subsequent consideration, since we did not want to impose an unquantified limit on signal-to-pink-noise (S/PN) that was stricter than the hard limit that we used—only those objects with an S/PN greater than eight were examined by eye. Approximately half of the total number of objects passed this limit. We wish to note that, at this stage, all of the objects were considered without respect to their cluster membership status. Although our initial S/PN threshold was set to eight, we found later that a higher threshold should be used, as detailed in Section 2.3.

2.3. Signal-to-pink Noise Threshold Determination

Given the residual systematic noise left in our data—largely leftover from the roll-correlated variability that was mostly (but not entirely) removed by our processing pipeline—we found S/PN to be a useful metric in evaluating signal significance. We used the S/PN as calculated by `VARTOOLS`, which is based on the definition of Pont et al. (2006). The signal value used in this calculation is the BLS transit depth, and the pink noise is a quadrature sum of the light curve white noise divided by the number of points in transit and the light curve red noise (calculated from the rms of the binned light curve with bin size equal to the transit duration) divided by the number of transits. After an initial search through the BLS search results, we saw transit-like signals that had lower S/PN than would be expected based on the observed white noise, suggesting a significant amount of correlated noise that could mimic transits. To better understand how well the correlated noise could mimic transits in our data, we reran our BLS search with the same parameters as before, but this time looking instead for "anti-transits," periodic box-shaped brightenings in the data instead of dimmings. Since there are no common periodic astrophysical phenomena that can produce such brightening signals at the ∼10 mmag level that Jupiter-sized planets produce for dimmings, these presumably are all due to noise. Gravitational self-lenses from binary systems consisting of a neutron star/black hole and a main-sequence star can produce such signals, but the occurrence rates for such objects are expected to be low; e.g., Masuda & Hotokezaka (2019) expect the *TESS* survey to have a detection rate of such objects of $\sim 10^{-4}$.

The by-eye vetting was performed again, with both the transit and anti-transit results presented. The light curves

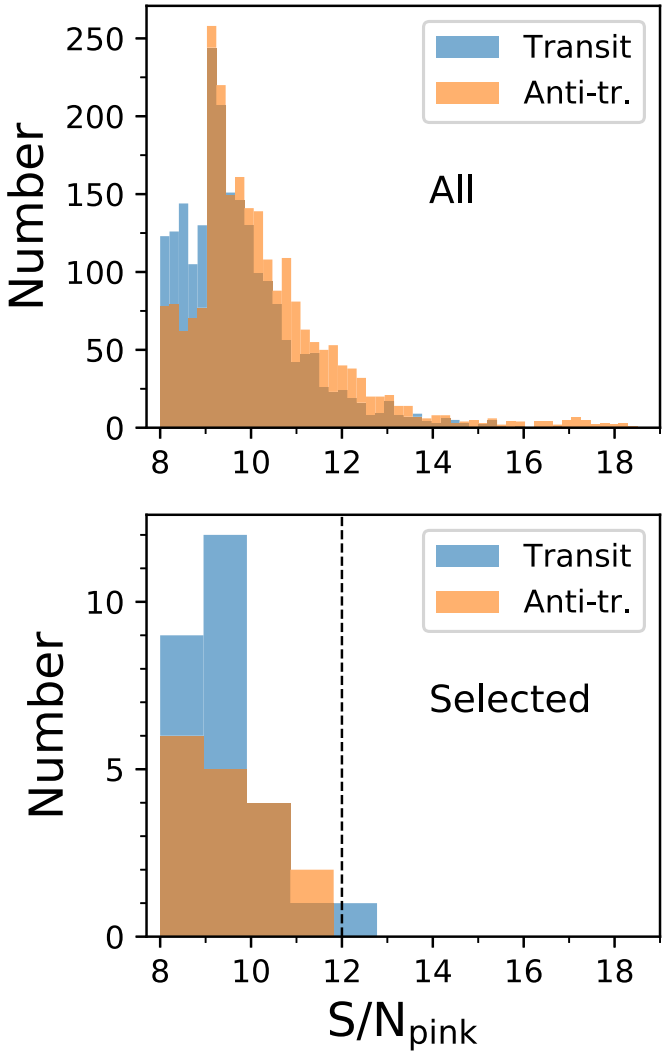

Figure 1. Histograms of signal-to-pink noise (S/PN) for all signals that exceed our thresholds and for our selected planet candidates. The distributions for the transits are shown in blue and the distributions for the anti-transits (labeled as "Anti-tr." in the figure) are shown in orange. Top panel shows all the values that cross our S/PN, transit duration, number of transits, and number of points in transit thresholds (see text). Bottom panel shows just those candidate signals that were selected in our by-eye vetting. The vertical line in the bottom panel shows our chosen S/PN cutoff value of 12.

presented for the anti-transit search results were inverted so that the signals would appear as transits. No special indication was given during the manual vetting as to whether a given signal was a transit or anti-transit, permitting a blind vetting of the signals. We implemented several cuts based on the BLS statistics. Only those signals with S/PN > 8, $q/q_{\rm exp} \geqslant 0.25$ (or 0.5, if $8 <$ S/PN < 9), number of transits $n_{\rm t} \geqslant 3$, and number of points in transit $n_{\rm pit} \geqslant 15$ were examined. We recorded all signals that we thought were possible transits, identifying 27 transits and 17 anti-transits as planet candidates (though here we call the anti-transits "planet candidates," we note that since these are not transits, they cannot be actual planet candidates). We then examined the distributions in S/PN for both the transits and anti-transits. These distributions are shown in Figure 1. A Kolmogorov–Smirnov (KS) test of the distributions for our 27 transit and 17 anti-transit planet candidates has a p-value of 0.51 and a KS statistic of 0.24, indicating that we cannot reject the hypothesis that the

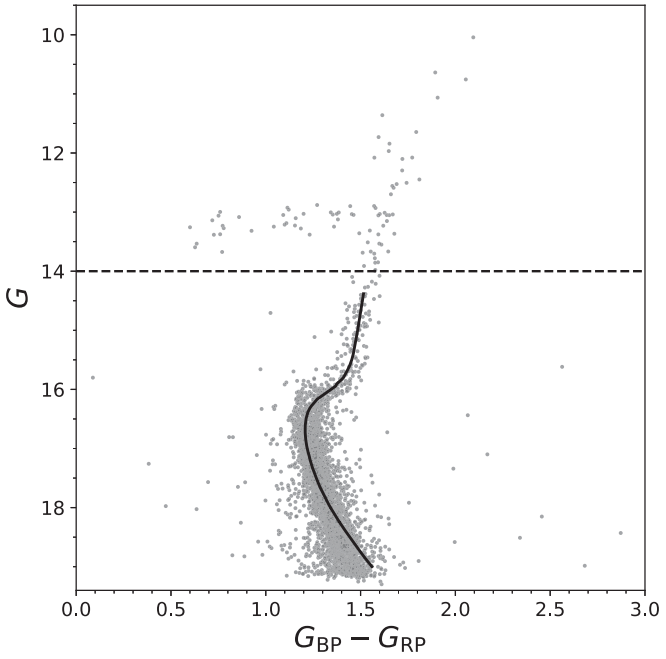

Figure 2. Color–magnitude diagram for objects in our analysis with a cluster membership probability >99%. The photometric data are taken from *Gaia* DR2 (Gaia Collaboration et al. 2018; Riello et al. 2018). The horizontal dashed line shows our magnitude cut for objects considered in our occurrence rate calculation, with objects below the line being included. The solid black line shows the isochrone fit used for transit injection and recovery, as described in the text.

planet-candidate transits and anti-transits are drawn from different distributions of S/PN.

Based on these results, it is possible our planet candidate signals are due to correlated noise and are thus false alarms. Despite this, we present our strongest candidates in Section 3. Based on our results, we decided that an S/PN cutoff value of 12 would be used in our transit–injection–recovery pipeline, to quantify our sensitivity to planetary transits. We do have one candidate with S/PN > 12, W2282, but with an S/PN value of 12.3, it is still only of marginal significance.

2.4. Occurrence Rate Calculation

We focused our occurrence rate calculation only on stars that are likely cluster members by including only those objects with membership probabilities greater than 99% as calculated by Wallace (2018) using *Gaia* DR2 proper motions. There were 3784 such objects. W2282, the S/PN > 12 star, is among the cluster members. For our occurrence rate calculation, we also decided to focus only on main-sequence and subgiant stars. We imposed a cutoff of $G > 14$ to focus on these objects, leaving us with 3704 objects for the calculation. Figure 2 shows a color–magnitude diagram (CMD) of the cluster members in our analysis with this cutoff indicated.

As a first step to calculating occurrence rates from our results, we quantified our transit detection efficiency. To do this, we injected transits into our light curves to test how well we could recover them. The transits were injected using `VARTOOLS`, based on the transit model of Mandel & Agol (2002). The injected periods and planet radii were taken from a 5×5 grid, with periods drawn uniformly from uniform bins in period between one and 36 days, and planet radii drawn log-uniformly from log-uniform bins between 0.3 and 2.0 $R_{\rm J}$.

The stellar radii and masses were determined from the PARSEC stellar evolution models (Marigo et al. 2017), obtained through the CMD v3.2 web interface,[3] this time making direct use of the *Gaia* DR2 G magnitudes and using the bolometric corrections for the *Gaia* bandpass from Maíz Apellániz & Weiler (2018). Through trial and error, we determined the best fit to the G versus $G_{\rm BP} - G_{\rm RP}$ CMD to be provided by a PARSEC isochrone with an age of 12.5 Gyr, a metallicity of [Fe/H] $= -1.2$, a distance of 1.8 kpc, extinction in the G band $A_G = 1.4$, and reddening $E(G_{\rm BP} - G_{\rm RP}) = 0.57$. This isochrone is shown in Figure 2. The stellar parameters were determined from the isochrone using just G magnitudes. There were seven objects with $14.0 < G < 14.28$ for which the isochrone interpolation as we had implemented it failed: W364, W642, W1643, W1898, W1912, W2757, and W3684 (using the identifiers from Wallace et al. 2019a). We exclude these objects from the occurrence rate calculation.

Random eccentricities, phases, longitudes of periapsis, and inclinations were chosen for each injected transit. Phases and longitudes of periapsis were chosen uniformly between zero and 2π; inclinations were chosen uniform in $\cos i$, subject to the constraint that transits actually occur; and eccentricities were drawn from a Beta distribution, with parameters as determined by the empirical fit of Kipping (2013) to his short-period planets. The planet mass was fixed at $0.8\,M_{\rm J}$ for all transit injections, independent of injected radius—as the simulated transit signal is effectively independent of the planetary mass. Limb darkening was incorporated with a quadratic model, using the parameters determined by Claret (2018) for *Kepler* using the PHOENIX-COND model (Husser et al. 2013).

The transit-injected light curves were then run through the same photometric processing as the light curves searched for planetary transits: decorrelation of systematic brightness variations against the telescope roll and TFA. Due to time constraints, we were unable to run a full BLS search for each transit-injected light curve. Instead, we used the `-BLSFixPer` option of `VARTOOLS` to perform a BLS search at only the injected period in order to get the BLS statistics. Our S/PN cut of 12 was applied, as well as the additional cuts used in our planet search (see Section 2.3), namely: $q/q_{\rm exp} > 0.25$, $n_{\rm t} \geqslant 3$, and $n_{\rm pit} \geqslant 15$. Using `-BLSFixPer` is effectively a conservative approach, as targets that have S/PN < 12 at the injected frequency but S/PN > 12 at other frequencies (such as a harmonic of the transit period) will be excluded in our search, whereas they may have been recovered in a full BLS search.

We ran some initial reconnaissance runs of our transit–injection–recovery pipeline with a coarser period–radius grid consisting of three period bins and four fixed planet radii and 12 samples from each bin. The periods were not sampled uniformly from each period bin, but rather from a range of the smallest periods in each bin. The purpose of these runs was to determine, star-by-star, parameter ranges in which we might expect to have a near-0% transit recovery rate. This information could then be used to accelerate the subsequent calculations. Applying just the S/PN cut and not the other cuts in $q/q_{\rm exp}$, $n_{\rm t}$, and $n_{\rm pit}$, we found 442 objects for which none of the 144 injected transits were recovered. Many of these objects were significantly blended with brighter and/or variable objects, and their light curves had very large scatter. These objects were removed from subsequent consideration—which, with the seven objects that were not fit by the isochrone, left us with 3255 objects that were included in our final transit–injection–recovery analysis. Additionally, for a given object, those period bin/planet radius pairs that had no recovered transits were recorded. Injected transits with periods equal to or longer and planet radii equal to or smaller than the values represented by these period bin/planet radius pairs were automatically recorded as nonrecoveries: about 50% of our injected transits were classified as such. If this approximation leads to us missing some injected transits that may have been recovered, then our final occurrence rate upper limits will be higher than we would have otherwise calculated, making this a conservative approximation for the upper limits.

We next injected 56 transits into each of the raw light curves for each radius–period bin in our 5×5 grid and ran them through our photometric processing pipeline. Recovered transits were then determined based on the BLS statistics and associated cuts as discussed. Then, for each radius–period bin, we calculated the number, N, of expected planets that we would have detected if every star hosted one planet in that bin, using (from, e.g., Ford et al. 2008)

$$N = \sum_{i}^{n_*} \frac{1}{n_i} \sum_{j}^{n_i} \delta_{ij} \frac{(R_{*,i} + R_{p,ij})(1 - e_{ij} \cos \varpi_{ij})}{a_{ij} \times (1 - e_{ij}^2)}, \qquad (1)$$

where i is an index over the stars examined, n_* is the number of stars examined, j is an index over the individual transit injections, n_i is the number of transit injections performed for the star, δ_{ij} is one if the particular injected transit is recovered and zero if not, $R_{*,i}$ is the stellar radius of the star i (based on the isochrone interpolation; this is the same stellar radius used for the transit injection), $R_{p,ij}$ is the radius of the planet for the given injected transit (taken as the actual value used for the transit injection rather than a calculated radius recovered from the transit signal), and e_{ij}, ϖ_{ij}, and a_{ij} are respectively the eccentricity, longitude of periapsis, and semimajor axis of the orbit of the injected transit. The quantity $(R_{*,i} + R_{p,ij})(1 - e_{ij} \cos \varpi_{ij}) / [a_{ij} \times (1 - e_{ij}^2)]$ accounts for the probability of transit given the random inclinations of orbits.

Once N is calculated for a given radius–period bin, the 3σ, 99.73% confidence interval upper limit for the occurrence rate assuming no detections is calculated using the binomial distribution, with N rounded to the nearest integer. For the bin in which our S/PN > 12 planet candidate falls, the 3σ confidence interval for the occurrence rate is also calculated. When calculating occurrence rates and limits for comparisons with other works, Equation (1) is again used to calculate the expected number of planets, but with injected transits chosen from a selected radius–period range instead of just the fixed bins we drew from for the transit injections.

In performing the calculation as we have, there is an implicit assumption that 100% of our injected transits would appear in the five highest BLS peaks in the full BLS search (since that is the number of peaks used in our planet search). There is also an assumption that 100% of injected transits that exceed our cutoff values would be identified in our by-eye analysis. We ran a full BLS calculation on a subset of our injected transits and found that 97.5% of injected transits that exceed our cutoff values appear in the five highest BLS peaks. We also performed a by-eye vetting of approximately 500 injected transits that exceed our cutoff thresholds with $12 <$ S/PN < 12.1, and found

[3] http://stev.oapd.inaf.it/cgi-bin/cmd

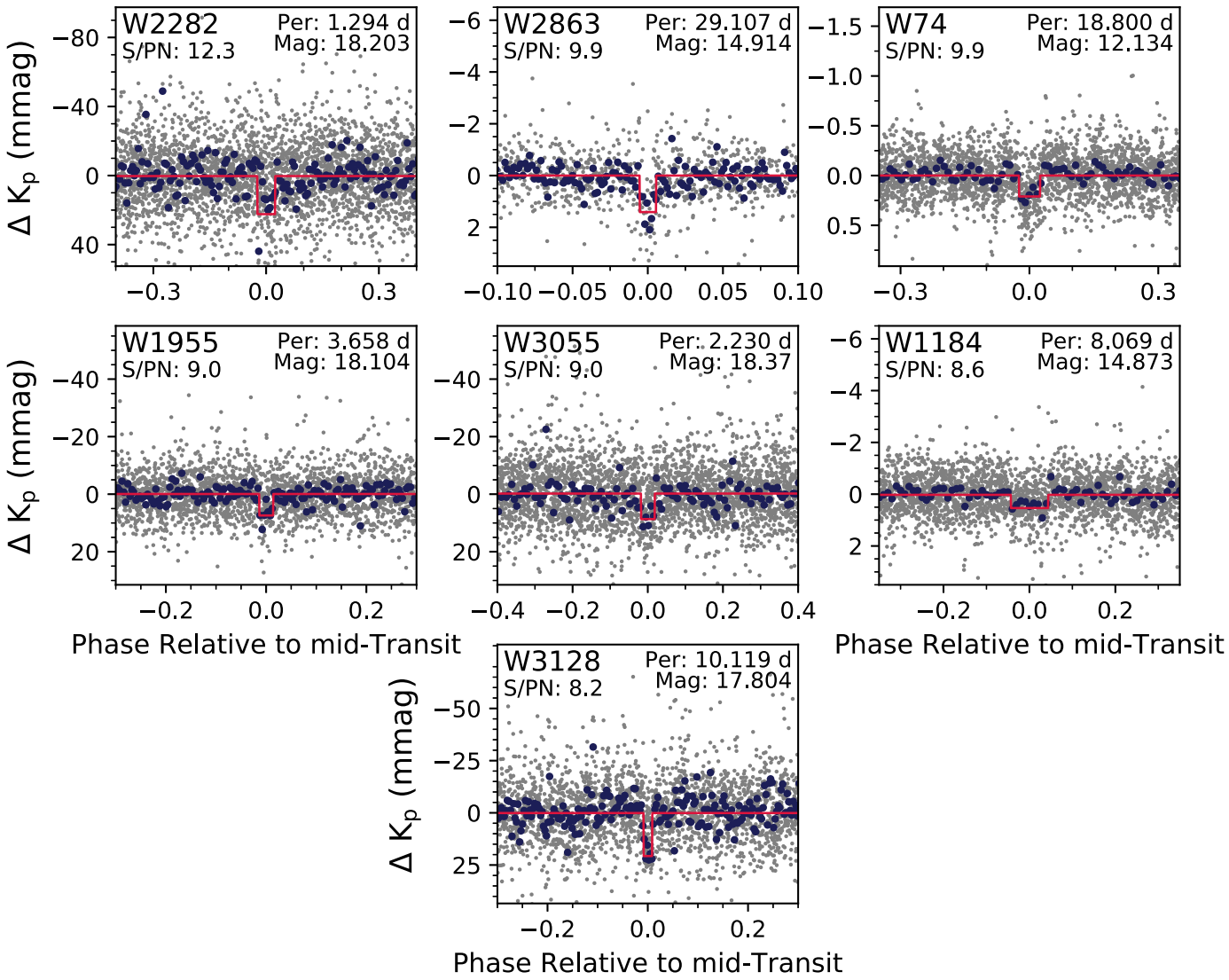

Figure 3. Phase-folded light curves for the transit signals of the best planet candidates. Each panel is for a different candidate. The upper left corner of each panel shows, from top to bottom, the object's identifier and the S/PN. The upper right corner shows, from top to bottom, the period in days and the median magnitude subtracted off for the light curve. In each panel, the gray points are the individual measurements (subject to a 5σ clipping with three iterations) and the blue points are binned-weighted-mean values. The red line shows the BLS fit to each phase-folded light curve.

Table 1
Information on Stars Hosting Planet Candidates

ID[a]	*Gaia* DR2 ID[b]	R.A.[c] (hh:mm:ss)	Decl.[c] (dd:mm:ss)	G[d] (mag)	Radius[e] ($R_\odot$)	Mass[f] ($M_\odot$)
W2282	6045466502667197056	16:23:34.95	−26:29:14.2	18.32	0.68	0.66
W2863	6045466640106160128	16:23:41.10	−26:28:04.2	15.07	3.4	0.80
W74	6045477635223138432	16:22:57.99	−26:28:46.8	12.30	13	0.86
W1955	6045503091478311808	16:23:31.71	−26:22:33.7	18.23	0.69	0.67
W3055	6045501996278191104	16:23:43.33	−26:25:06.1	18.57	0.64	0.64
W1184	6045478597295755520	16:23:22.89	−26:27:04.2	15.02	3.5	0.80
W3128	6045466429642662272	16:23:44.26	−26:29:12.0	18.13	0.71	0.68

Notes. All of these stars are proper motion cluster members (Wallace 2018).
[a] The identifier by which the object is known in this work, the same as in Wallace et al. (2019a).
[b] *Gaia* DR2 source ID.
[c] J2000.0; data taken from *Gaia* DR2 (Lindegren et al. 2018).
[d] *Gaia* G magnitude from *Gaia* DR2 (Riello et al. 2018).
[e] The radius of the star in units of solar radii, determined from an isochrone fit.
[f] The mass of the star in units of solar mass, determined from an isochrone fit.

Table 2
Information on Planet Candidates

ID[a]	Period[b] (days)	T_0[c] (KBJD)	Depth[d] (mmag)	Radius[e] (R_J)	q[f]	q/q_{exp}[g]	S/PN[h]
W2282	1.2937 ± 0.0014	2061.955 ± 0.040	22	1.0	0.047	0.82	12.3
W2863	29.07 ± 0.86	2078.65 ± 0.67	1.4	1.3	0.011	0.36	9.9
W74	18.804 ± 0.057	2071.675 ± 0.077	0.21	1.9	0.049	0.33	9.9
W1955	3.6608 ± 0.0020	2062.6319 ± 0.0068	7.5	0.62	0.028	1.0	9.0
W3055	2.20858 ± 0.00054	2062.1311 ± 0.0063	8.9	0.62	0.037	1.0	9.0
W1184	8.08 ± 0.10	2066.84 ± 0.28	0.51	0.82	0.087	1.2	8.6
W3128	10.118 ± 0.090	2063.465 ± 0.094	21	1.1	0.017	1.1	8.2

Notes. All of these stars are proper motion cluster members (Wallace 2018).
[a] The identifier by which the object is known in this work, the same as in Wallace et al. (2019a).
[b] The period of the transit signal in days.
[c] The time of transit center in KBJD.
[d] The depth of the transit signal in millimagnitudes.
[e] The calculated radius of the planet in Jupiter radii based on the transit depth and isochrone-based stellar radius.
[f] The fractional transit duration.
[g] The ratio of the fractional transit duration with the expected $b = 0$ transit duration.
[h] The S/PN of the signal.

98.8% passed our vetting. Presumably, an even larger fraction of those with higher S/PN values would pass the by-eye vetting. Based on these results, we decided to maintain our assumption of 100% recovery for both of these steps.

3. Transit Search Results

Figure 3 shows the phase-folded light curves of our seven most promising planet candidates. We choose not to present the other 20 candidates that initially passed our by-eye vetting, as we now consider these to almost certainly be false alarms. Table 1 presents information on the stars hosting these planet candidates, and Table 2 presents information for each of the transit signals and calculated planet properties. The uncertainties on the periods and times of transit center were calculated using a Markov chain Monte Carlo fit of the transit models of Mandel & Agol (2002) to the data. All of the planet candidates presented are proper motion members of the cluster (Wallace 2018). Except for W2282, all of these objects fall below our S/PN threshold of 12, and W74 is brighter than our G threshold of 14. Owing to the potential scientific impact of discovering a transiting exoplanet in a GC, we choose to present the most promising candidates we found, irrespective of these cuts. That being said, the relatively low S/PN values these signals have indicates that most, if not all, of these candidates are likely false alarms. The phase-folded light curves of W74, W1184, W2863, and W3128 appear to be the most robust of the seven, while the other three appear less robust. Given the high probability that these signals are false alarms, follow-up is needed before they are confirmed. The next step in following these up would be to confirm the transits and then look for background objects to ensure these objects are not blended eclipsing binaries. For $\sim$1 R_J objects, additional RV follow-up would be needed to measure the masses in order to identify them as planets, brown dwarfs, or late M-dwarfs. For Neptune-sized objects and smaller, the follow-up photometric data may be sufficient to classify the objects as planets without RV data. This is because there are no known astrophysical objects with radii comparable to Neptune orbiting stars, so if the data permit a sufficiently precise measurement of the radius of a Neptune-sized object and are able to rule out blended eclipsing binaries (e.g., by showing a lack of secondary eclipses and ellipsoidal variability), direct confirmation from the transit data alone is possible.

Owing to the crowded nature of the cluster and of the *K2* observations in particular, blending is a virtually unavoidable aspect of the data. We confirmed that W1184, W1955, W2282, W3055, and W3128 had the largest signal amplitudes of all nearby objects at the respective transit periods, for those objects for which we had light curves. The results for W74 and W2863 were more ambiguous, likely owing to their brighter magnitudes causing these stars to impact larger areas of the images than the other fainter stars. However, these two stars are each the brightest stars in their respective areas of the images.

W74 merits some additional comments. Its CMD position puts it on the red giant branch and it is asteroseismically active. A Generalized Lomb–Scargle (GLS) (Lomb 1976; Scargle 1982) search reveals significant sinusoidal variability at a variety of periods (though not the $\sim$19 days found by BLS), with the strongest variability at 0.77 and 1.69 days. Prewhitening the light curve by running LS three times and removing a two-harmonic and one-subharmonic fit to the peak period each time prior to running BLS recovers a similar period, 18.843 days, and a comparable (though lesser) S/PN value of 9.6. It also bears mentioning that the $\sim$18.8 day period of this object, based on our Yi et al. (2001) isochrone fit for the mass and radius of the star, has a semimajor axis of $\sim$28 $R_\odot$, compared to the calculated stellar radius of $\sim$13 $R_\odot$. This is a physically plausible scenario, but again this is a blended object and we were not able to conclusively determine whether the transit belonged to this object. A blended eclipsing binary scenario is also possible. The implied planet radius based on the calculated stellar radius is 1.9 R_J.

A few of our "planet candidate" anti-transits are shown in Figure 4 as examples of the kinds of false alarms the correlated noise in our light curves can produce. While the S/PN values are comparable to those of our prospective planet candidates, we think that a qualitative, by-eye evaluation of the signals

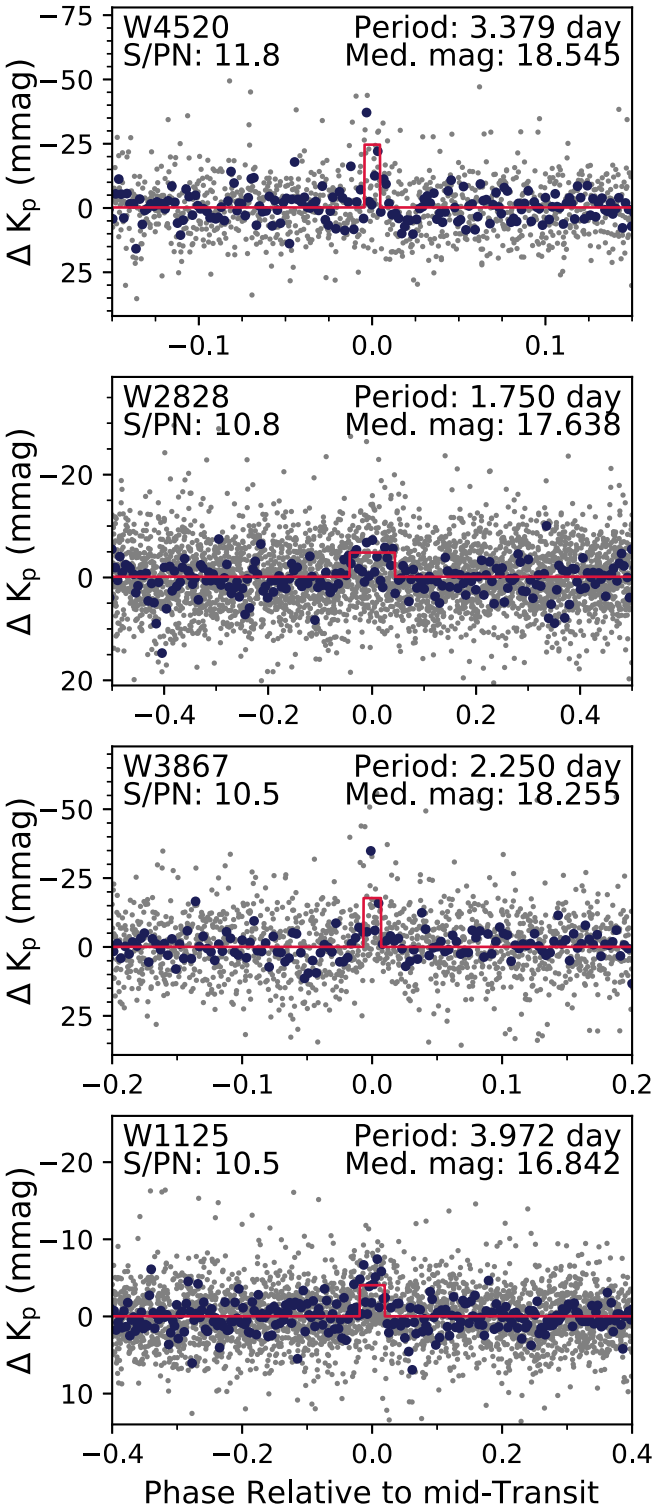

Figure 4. Same as Figure 3, but for a few representative anti-transits. These are presented as examples of the false alarms that can be produced by the systematic noise that exists in our data.

shows W74, W1184, W2863, and W3128 in particular to be more physical and transit-like than even the highest S/PN anti-transits. Also, those four objects have much longer periods than any of the anti-transits we identified, suggesting that the transit-mimicking correlated noise may exist only at shorter periods

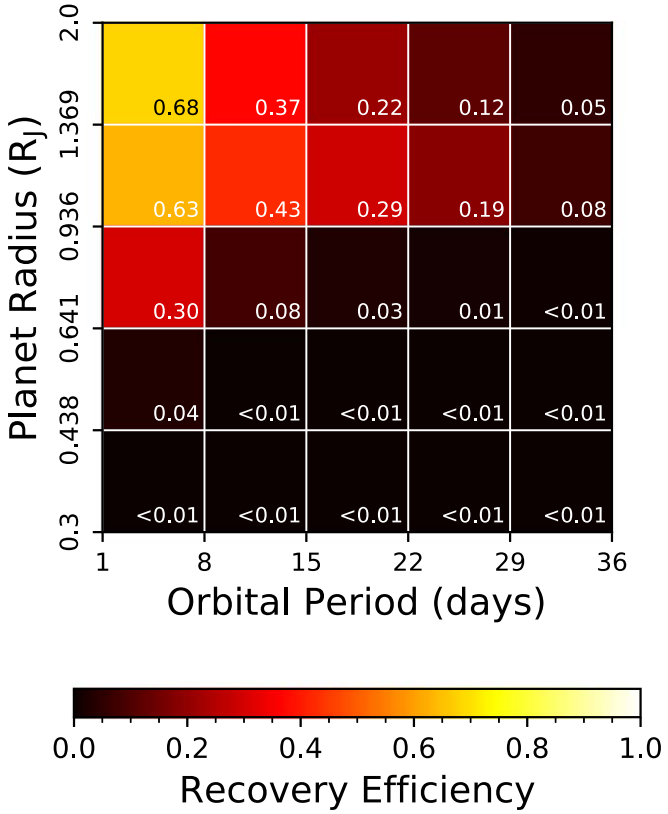

Figure 5. Recovery efficiency of our transit–injection–recovery pipeline. Each bin shows the fraction of injected transits that were successfully recovered across all the stars. The number in the lower right corner of each bin shows the efficiency value, which is also represented by the color of the bin and the associated color bar. In cases where the recovery efficiency was less than 1%, an upper limit of 1% is shown.

and that these longer-period signals may be more likely to be real.

4. Occurrence Rate Results

4.1. Transit Recovery Results

Figure 5 shows the recovery efficiency of our injected transits across our radius and period bins. We define recovery efficiency as the fraction of transits that were successfully recovered; in Figure 5, this is the efficiency across all of the injected transits and all of the stars. As would be expected, the recovery efficiency trends toward higher values for larger planets and smaller orbital periods. Of note, though, is that for period bins greater than eight days, the recovery efficiency is higher for our second-largest planet radius bin (∼0.9 to ∼1.4 R_J) than for our largest planet radius bin (∼1.4–2 R_J). A possible explanation for this is that the deeper transits produced by the larger radius planets were more likely to be distorted and diminished by our photometric processing pipeline than the shallower transits from 0.9 to 1.4 R_J planets. The shorter-duration transits at smaller periods may be less likely to be impacted by the processing pipeline, which would explain the higher recovery efficiency seen for the larger planets for periods shorter than eight days. Also, we found that some of the deepest transits had the bottom portions of the transits trimmed by the sigma clipping. Such transits were still detectable by

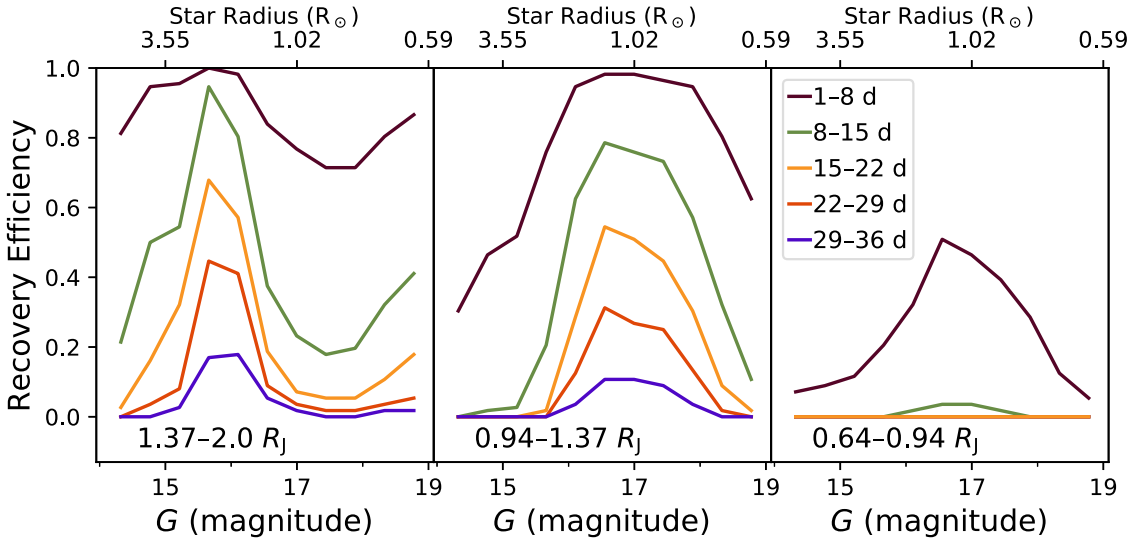

Figure 6. Recovery efficiency of our transit–injection–recovery pipeline, broken down by stellar magnitude and bins of injected planet radius and orbital period. Magnitude is represented along the horizontal axis, planet radius by the three panels, and orbital period by the color. The lines show the median recovery efficiency as a function of magnitude across all stars for a given radius–period bin. In the rightmost panel, the 22–29 days (red) and 29–36 days (blue) lines fall behind the 29–36 days (yellow) line, and thus do not appear. The planet radius range for each panel is indicated in the bottom of the panel. The legend in the rightmost panel shows the color representation of the orbital period bins ("d" in the legend stands for "day") and applies to all three panels. The top axis of each panel shows G converted to stellar radius via an isochrone fit.

BLS but had a lower S/PN due to the diminished apparent transit depth.

Figure 6 shows the recovery efficiency broken down by G magnitude, orbital period, and planet radius. We see (as expected) that shorter-period planets have a higher recovery efficiency than longer-period planets. We also see lower recovery efficiencies for the brightest stars relative to the peak efficiencies reached (usually around $G \approx 16$–17). This is due to the large radii of the brightest stars (see top axis of Figure 6) diminishing the transit depth—and thus, the signal size and recoverability as well. In the leftmost panel of Figure 6, corresponding to the largest-radius injected planets, we also note that detection efficiencies tend to be higher at both $G = 16$ and $G = 19$ than at $G = 18$, particularly in the period range of 1–15 days. The nonmonotonic variation in detection efficiency with magnitude is due to the different magnitude dependencies of two competing effects. Brighter stars in the cluster have higher-precision light curves, which tend to increase the signal to noise of the transits. However, fainter stars in the cluster have smaller stellar radii, which leads to deeper transits for a given planetary radius. In the middle and rightmost panels of Figure 6, this increase in recovery efficiency at the faintest magnitudes is not seen. In the rightmost panel, we see a large drop in recovery efficiency overall for 0.64–0.94 R_J planets relative to the other two panels—the larger radii planets.

4.2. Planet Occurrence Rates and Limits

We now present our calculated occurrence rate limits and compare with other published occurrence rates. Figure 7 shows the calculated occurrence rate upper limits across our radius–period bins, and in the case of the bin containing our single S/PN > 12 planet candidate (W2282), the range for the occurrence rate if the planet candidate is real. For our shortest-period bins, we are able to get down to limits of 1.6–3.5% for bins with planet radius larger than 0.64 R_J. To put these limits in context, Table 3 compares our occurrence rate limits with those of works using *Kepler*, *TESS*, or RV surveys

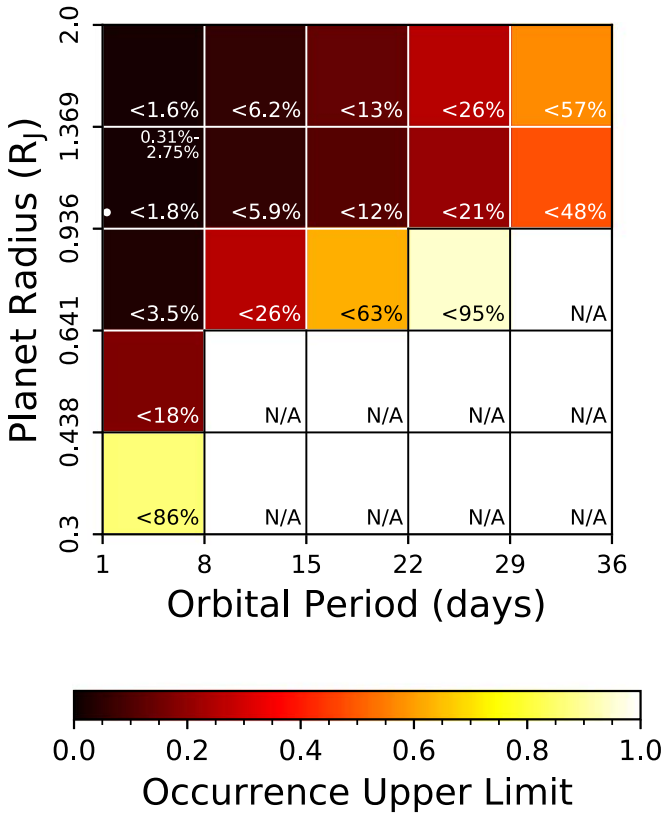

Figure 7. Calculated upper limits on occurrence rates for our radius–period bins. The lower right hand of each bin shows the 3σ upper limit in the fraction of stars having at least one planet in that bin as calculated using a binomial distribution based on our determined detection efficiencies and transit probabilities. Those bins marked "N/A" either had detection efficiencies too low for us to calculate any occurrence rate, or had a rate that was indistinguishable from 100%. The color of each bin is a representation of the occurrence rate upper limits, based on the color bar at the bottom of the figure. The white point represents the one planet candidate we found that passes our S/PN threshold, W2282, and the range in the upper-right corner of the associated bin is the 3σ range on the occurrence rate assuming the planet candidate is real.

Table 3
Comparison with *Kepler*, *TESS*, and RV Occurrence Rates for Field Stars

Per. Range[a] (days)	Rad. Range[b] (R_J)	References	Published Rate[c]	Our Upper Limit[d]	Our Rate[e]
		Kepler Studies			
0.8–10	0.71–2.85	Howard et al. (2012)	0.4% ± 0.1%	<2.2%	0.38–3.3%
0.8–50[f]	0.71–2.85	Howard et al. (2012)	1.3% ± 0.2%	<6.1%	1.1–9.1%
0.8–10	0.36–0.71	Howard et al. (2012)	0.5% ± 0.1%	<16%	⋯
0.8–10	0.54–1.96	Fressin et al. (2013)	0.43% ± 0.05%	<2.6%	0.44–3.9%
0.8–17	0.54–1.96	Fressin et al. (2013)	0.70% ± 0.08%	<3.8%	0.66–5.7%
0.8–29	0.54–1.96	Fressin et al. (2013)	0.93% ± 0.10%	<6.0%	1.0–8.9%
0–10	0.8–2	Masuda & Winn (2017)	$0.43^{+0.07}_{-0.06}$%	<2.1%	0.36–3.2%
0–10	0.8–2	Masuda & Winn (2017)	$0.24^{+0.10}_{-0.09}$%[g]	<2.1%	0.36–3.2%
1–10	0.71–2.14	Petigura et al. (2018)	$0.57^{+0.14}_{-0.12}$%	<2.2%	0.38–3.3%
		TESS Study			
0.9–10	0.8–2.5	Zhou et al. (2019)	0.41% ± 0.10%	<2.1%	0.36–3.2%
		RV Studies			
0–11	0.72–2[h]	Mayor et al. (2011)	0.89% ± 0.36%	<2.4%	0.40–3.5%
0–10	0.55–2[h]	Wright et al. (2012)	1.20% ± 0.38%	<2.5%	0.44–3.8%

Notes.
[a] The period range used in the comparison work for the occurrence rate calculation. Note that the smallest period used in this work is one day, and so our calculation truncates smaller period ranges at one day.
[b] The planet radius range used in the comparison work for the occurrence rate calculation. Several references used $R_\oplus$ as their unit of radius; these values have been converted to R_J and rounded. Note that the largest radius examined in this work is 2 R_J, and so our calculation truncates larger radius ranges at 2 R_J.
[c] The comparison work's planet occurrence rate as published.
[d] Our calculated occurrence rate upper limit for the same period and radius range.
[e] Our calculated occurrence rate assuming W2282 is a planet. This value is not included if W2282 does not fall in the given period and radius ranges.
[f] Our calculation truncates at 36 days.
[g] For this value, Masuda & Winn (2017) restricted their analysis to the *Kepler* stars that were in the same range of masses as the stars search in 47 Tuc for planets by Gilliland et al. (2000).
[h] These were limits in mass rather than radius. We converted the lower mass limit to a radius using the empirical relation derived by Chen & Kipping (2017), and imposed our default upper limit of 2 R_J.

Table 4
Comparison with Globular Cluster Occurrence Rates

Per. Range[a] (days)	Rad. Range[b] (R_J)	References	Published Rate[c]	Our Upper Limit[d]	Our Rate[e]
1–8	0.64–2	Gilliland et al. (2000)[f]	$\lesssim$0.7%	<2.1%	0.35–3.1%
1–16	1–2	Weldrake et al. (2005)	⋯	<2.7%	0.47–4.1%
1–5[g]	1.5–2[g]	Weldrake et al. (2008)	<1.7%	<0.81%[h]	⋯
1–14[i]	0.94–1.37[i]	Nascimbeni et al. (2012)	<9.1%	<0.93%[h]	0.31–1.7%

Notes.
[a] The period range used in the comparison work for the occurrence rate calculation.
[b] The planet radius range used in the comparison work for the occurrence rate calculation. The radius ranges used were not always clear in the comparison works, so we made our best guess, taking into account our radius–period grid boundaries. Note that the largest radius examined in this work is 2 R_J, and so our calculation truncates larger radius ranges at 2 R_J.
[c] The comparison work's planet occurrence rate upper limit as published.
[d] Our calculated occurrence rate upper limit for the same period and radius range.
[e] Our calculated occurrence rate assuming W2282 is a planet. This value is not included if W2282 does not fall in the given period and radius ranges.
[f] Provided courtesy of K. Masuda (2019, private communication) based on the work in Masuda & Winn (2017). The calculated 3σ occurrence rate upper limit is based on the same stellar mass range described in Table 3, note g.
[g] The published rate is for their 1–5 day calculation; we performed our calculation over 1–8 days to guarantee at least one of our radius–period bins be included. Similarly, the quoted rate is only for >1.5R_J objects, but we had to use 1.37–2 R_J objects to cover a whole bin.
[h] The 95% confidence instead of our typical 3σ, to match the confidence level used by both Weldrake et al. (2008) and Nascimbeni et al. (2012).
[i] The upper end of the period range was arrived at dividing their total observation duration (28 days) in half; planet radius range was chosen to span their single injected planet radius, 1 R_J.

for field stars. These previous works are: *Kepler*-based occurrence rates from Howard et al. (2012), Fressin et al. (2013), Masuda & Winn (2017), and Petigura et al. (2018); a *TESS*-based occurrence rate from Zhou et al. (2019); and RV occurrence rates from Mayor et al. (2011) and Wright et al. (2012). Table 4 compares our occurrence rate limits with those of previous GC planet searches: Gilliland et al. (2000) and Weldrake et al. (2005) for 47 Tuc, Weldrake et al. (2008) for ω Cen, and Nascimbeni et al. (2012) for NGC 6397.

As seen in Table 3, in no case were we able to set an upper limit that shows an occurrence rate smaller than what we would expect from the field population. Furthermore, even if W2282 or a comparable planet candidate in the HJ regime is shown to actually be a planet, most of the *Kepler*- or *TESS*-based occurrence rates would be consistent with the lower end of our calculated occurrence rate ranges, though the upper ends of our ranges are inconsistent in all those cases. Thus, based on these previous studies, and ignoring the metallicity dependence of HJ occurrence as seen in the field, we would expect to have a nonvanishing probability of finding a planet. Comparing with the RV studies, the RV rates fall within our W2282-based occurrence rate ranges, also suggesting from these results that there is some meaningful, if small, probability of finding a planet.

Comparing with the previous searches in GCs, and focusing first on the 47 Tuc surveys because those were the most constraining, Masuda & Winn (2017) showed that Gilliland et al. (2000) should have found $2.2^{+1.6}_{-1.1}$ planets in their survey, and that Weldrake et al. (2005) should also have found $\sim$2 planets in their survey. Thus, their results (possibly) show a lower occurrence rate in 47 Tuc than found by *Kepler* for the field population for the period ranges searched. Our results do not reach such a constraining level for HJs. However, our sensitivity reaches further in planet radius and period than either of those two previous surveys. Our $\sim$78 day baseline and the nearly continuous nature of the observations would virtually guarantee us three visible transits for orbital periods up to $\sim$26 days—and for some cases, out to $\sim$39 days. This is compared to the 8.3 day baseline of Gilliland et al. (2000) and the 33 day baseline of Weldrake et al. (2005). In addition, Gilliland et al. (2000) were insensitive to nearly all planets with a radius below 0.8 R_J, and had at best 40% recovery of 1 R_J objects for the optimal stellar magnitude. Our work is still reasonably sensitive down to $\sim$0.6 R_J for small periods, and somewhat sensitive down to $\sim$0.4 R_J.

In Table 4, we do have a more constraining upper limit than the work in ω Cen by Weldrake et al. (2008) for their very limited period and radius range. We also improve on the limit determined by Nascimbeni et al. (2012). They were able to put a (95% confidence) upper limit of 9.1% on the occurrence of $\sim$1 R_J objects with periods between 1 and $\sim$14 days, while we are able to put an upper limit of 0.93% for the same period range and a similar planet radius range at the same confidence level. Weldrake et al. (2005) did not provide any quantification of their sensitivity to planet radius, but their calculations assumed a relatively large radius of 1.3 R_J, and we assume they were sensitive to planets of that radius and larger.

The primary contribution of this work is the new parameter range it explores for planet occurrence rates in GCs, in both planet radius and orbital period. The occurrence rate limits in these new parameter ranges ($0.3 \lesssim R_p \lesssim 0.8\ R_J$ at short periods and $P \lesssim 36$ days for large-radius planets) are shown in Table 3, in comparison with the field occurrence rates. In particular, we set occurrence rate upper limits of 16% for 0.36–0.71 R_J planets with 1–10 day periods and 6.1% for 0.71–2 R_J planets with 1–36 day periods. While these numbers may not seem impressive when compared to the equivalent occurrence rates determined from *Kepler* ($0.5\% \pm 0.1\%$ for 0.36–0.71 R_J planets with 0.8–10 day periods and $1.3\% \pm 0.2\%$ for 0.71–2 R_J planets with 1–50 day periods; Howard et al. 2012), these are the first limits set for planets in a GC in these period and radius regimes. These limits demonstrate that the occurrence of planets in M4 just outside the HJ regime (in terms of period or radius) is not ubiquitous—and, for the 0.71–2 R_J, 1–36 day range, is at most a factor of about five higher than has been found for the field population.

5. Discussion

This work represents the first look at a planet occurrence rate for the GC M4, and the fifth photometry-based examination of a planet occurrence rate for a GC. It is worth noting that, although our results do not place very stringent constraints on the occurrence of planets in M4, *Kepler* was not designed or optimized for looking at GCs—in particular, the $\sim 4''$ pixel^{-1} image resolution led to significant blending in the images—and the superstamp observations of M4 were originally intended for observing RR Lyrae variables. Obtaining even the level of constraints we did from a telescope and observations not originally intended for a GC planet search is yet another demonstration of an unanticipated scientific result from *Kepler*.

Though our constraints cannot rule out planet occurrence rates for M4 matching those of the field stars, given the current uncertainties on planet formation—particularly the formation of close-in giant planets—and uncertainties on GC formation, obtaining any constraints on planet occurrence in GCs for new regimes of planet radius and period is useful. It may be that the occurrence of certain kinds of close-in planets in GCs is more common due to some unique aspect of GCs.

There are some reasons we might expect the occurrence of close-in planets to be higher in a GC than in the field. For example, Hamers & Tremaine (2017) demonstrated that the increased number of close stellar encounters experienced by GC stars over their lifetimes could enhance the HJ occurrence rate for certain stellar densities (peak formation occurred at a density of $\sim 4 \times 10^4$ pc^{-3}) if HJs are formed through high-eccentricity migration. The formation of GCs themselves is still something of a mystery (see Gratton et al. 2012 for a review), and perhaps there is something unique about the formation of stars in GCs that would increase the formation of close-in planets. Our results, along with those of the previous GC planet occurrence works, provide constraints on just how enhanced a planet occurrence rate might be, should there indeed be enhanced close-in planet formation in GCs.

On the other hand, much work has been done to show why specifically HJ occurrence in GCs might be suppressed. The occurrence of HJs is known to correlate with host star metallicity (e.g., Fischer & Valenti 2005), and this has been used to argue that the low metallicities of GCs would inhibit HJ formation. For example, Santos et al. (2001) showed the known metallicity dependence as being able to explain the 47 Tuc planet nondetection of Gilliland et al., but the reason behind a metallicity–occurrence connection is not well understood. It may be that the underlying cause of this connection does not apply in the unique environments of GCs. Additionally, the

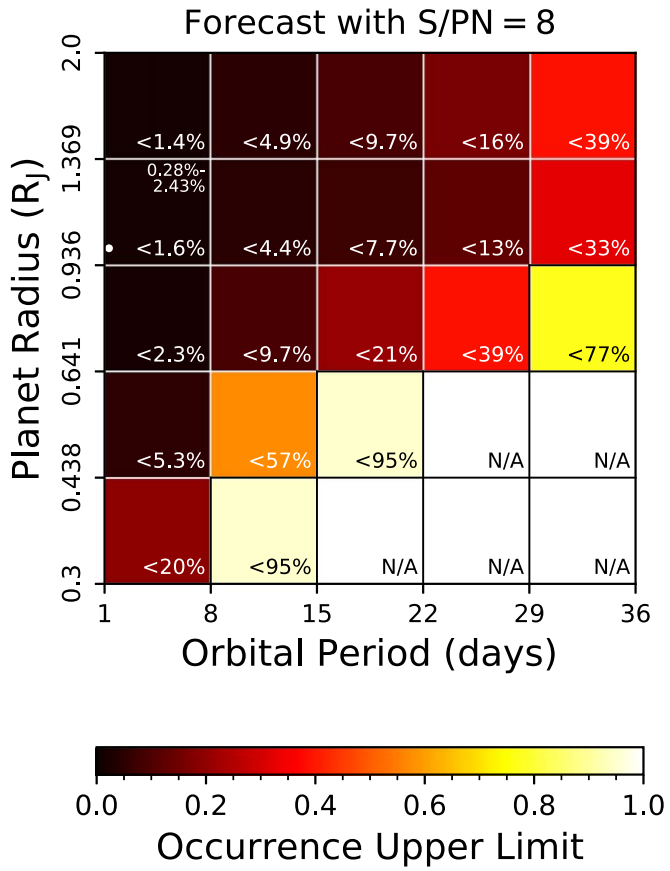

Figure 8. Same as Figure 7, but instead showing a forecast of the limits that could be set if an S/PN threshold of 8 was able to be used instead of 12 and no additional planet candidates were found.

dense stellar environment of GCs and the associated levels of radiation from particularly the nearby massive stars may inhibit giant-planet formation (Armitage 2000; Adams et al. 2004; Thompson 2013). Furthermore, in addition to enhancing the rate of close-in planets, dynamical interactions with passing stars can also remove planets from planetary systems (Sigurdsson 1992; Bonnell et al. 2001; Davies & Sigurdsson 2001; Fregeau et al. 2006; Spurzem et al. 2009), particularly planets on wide orbits. Interactions between stars and protoplanetary disks lead to decreases in disk sizes as well (Breslau et al. 2014). Until better constraints or actual occurrence rates are determined for GCs, for a larger range of planet radii and orbital periods than are presently accessible from existing data, it will be difficult to determine the precise impact a GC environment has on planet formation and occurrence.

As an analysis of how an improvement on our light curves and/or noise characterization and removal could improve our occurrence rate limits, we show a forecast in Figure 8 of the limits that would be set if an S/PN threshold of 8 (instead of 12) could be imposed, assuming no planets were found. W2282 and the associated occurrence rate is still included for comparison with Figure 7. Our upper limits in the HJ regime would not improve by very much, but we would be able to place more stringent constraints for $0.64\,R_J \lesssim R_p \lesssim 0.94\,R_J$ across all the periods examined, and for $0.3\,R_J \lesssim R_p \lesssim 0.64\,R_J$ for the shortest periods examined here. Even if our limits in the HJ regime do not improve much, a better understanding of the noise would allow for an improved vetting of the current planet candidates.

As limited as our constraints are, they may be the best to come for a while. The only near-term continuous photometric survey is *TESS*, but with its $\sim 20''$ pixel^{-1} image resolution, it will leave most of the stars in GCs hopelessly blended. Moreover, the $\sim$1 month observation span most of its survey field will be covered by is only about a third the span of what is available in this work with *K2*. An *HST* campaign similar to that of Gilliland et al. (2000) for M4—being about half the distance as 47 Tuc—should permit a factor of two increase in the signal-to-noise ratio for stars of comparable masses and evolutionary state as in 47 Tuc; a campaign along these lines might be considered. The main limiting factor in setting the HJ occurrence limit from the *K2* data is the relatively small number of cluster stars observed, i.e., $\sim$4000 compared to $\sim$34,000 GC stars in Gilliland et al. (2000) and $\sim$20,000 GC stars in Weldrake et al. (2005). The *K2* superstamp covered a relatively small fraction of the stars in the cluster, so a survey that covers more of the cluster could be useful.

Despite the low S/PN of our planet candidates, given the scientific impact of discovering and characterizing a transiting planet in a GC, we argue that it is worth the effort to confirm whether these are real planet signals.

Unfortunately, the data are already five years old. Referencing Table 2, the transit timing uncertainties for W2863 (0.67 day) and W1184 (0.28 day) are considerable. Taking the number of transits that are expected to have occurred in the last five years and multiplying by the period uncertainties as an approximate calculation of additional uncertainty on transit timing arising from the period uncertainties, we get: W2282, 2.0 days; W2863, 54 days; W74, 5.5 days; W1955, 1.0 day; W3055, 0.45 day; W1184, 23 days; and W3128, 16 days. Thus, only for W74, W1955, and W3055 would the transit epoch number be known with certainty if a transit were to be observed five years on. In no case is the present transit timing known with sufficient precision to be sure of catching a transit in one night's observation, so an extended follow-up campaign would be needed. In this, the crowded nature of the cluster and the manageably sized field of view of the *K2* superstamp ($\sim 10'$ by $\sim 20'$) are advantages. Many available wide-field imagers can cover a large fraction of (or even the entire) superstamp, allowing for simultaneous observation of more than one planet candidate, and the data would also have the advantage of observing other interesting variables guaranteed to be present; see Wallace et al. (2019a) for a catalog.

6. Conclusion

We searched for transiting planets in the GC M4 using data from the *K2* mission. These data represent the longest continuous observation of a GC, permitting a search for the longest-period planets ever searched in a GC. The data are also of sufficient quality to be sensitive to planets of smaller radii than any previous transit search in a GC. From 3784 light curves extracted from the data, with a maximum observation duration of $\sim$78 days, and using a BLS transit search followed by a by-eye vetting, we identified 27 planet candidates in the data. An analysis of the systematic noise in the light curves revealed that an S/PN cutoff value of 12 should be used to remove probable false positives, with only one of the planet candidates exceeding this cutoff value, yet there still remains uncertainty as to whether this might be a false alarm. Despite

this, we present information on this and six of our other most promising candidates. The light curves are publicly available at Wallace et al. (2019b).

We calculated 3σ occurrence rate upper limits based on a nondetection of planets and occurrence rate ranges assuming our S/PN > 12 planet candidate as real, for a variety of period and planet radius ranges. Comparing these limits and rates to the literature, for previous GC works, we find a factor of two lower occurrence rate limit than was calculated by Weldrake et al. (2008) for ω Cen for $R_p > 1.5R_J$ objects. We also improve on the Nascimbeni et al. (2012) limit for $\sim$1 R_J planets with $\lesssim$14 days orbits, obtaining a 2σ limit of $<0.93\%$. Using a similar period (1–8 days) and radius range (0.64–2R_J) as those to which the landmark study of Gilliland et al. (2000) was sensitive, our limit was $<2.1\%$, compared to the $<0.7\%$ limit determined by Masuda & Winn (2017) using the Gilliland et al. (2000) data. Comparing with occurrence rates calculated from field star transit surveys, our HJ occurrence rate limits are factors of about four to six larger than the *Kepler* and *TESS* rates. Similarly, for RV studies, our HJ occurrence limits are about a factor of two higher than the rate of Wright et al. (2012), and about a factor of three higher than the rate of Mayor et al. (2011). Our rate upper limits for longer-period orbits ($\gtrsim$15 days) of $\sim 1\,R_J$ objects and for smaller planets ($\sim 0.4\,R_J$ and larger) are much larger than the rates known for those regimes from *Kepler*, and are not very constraining, but are the first such limits ever set for a GC.

Future work that could be done to build off these results includes photometric follow-up of the planet candidates to confirm the transits, and improving the systematic noise characterization and abatement in the light curves to permit greater sensitivity to lower S/PN transits. Lowering the S/PN threshold would allow us to put significantly better constraints on $P \lesssim 8$ days planets with $0.3\,R_J \lesssim R_p \lesssim 0.6R_J$ planets, and for $0.6\,R_J \lesssim R_p \lesssim 0.9R_J$ planets across all periods examined.

We thank Kento Masuda for his occurrence rate calculation, Waqas Bhatti for assistance with `astrobase`, and Fei Dai and Josh Winn for providing a second vetting of our planet candidates and useful comments. We also thank Wojtek Pych for assistance in procuring and using the Cluster AgeS Experiment (CASE) light curves for M4, though the data did not ultimately make it into the final work. J.H. and G.B. acknowledge funding from NASA grant NNX17AB61G. This research includes data collected by the *Kepler*/*K2* mission and obtained from the MAST data archive at the Space Telescope Science Institute (STScI). Funding for the *Kepler* mission is provided by the NASA Science Mission Directorate. STScI is operated by the Association of Universities for Research in Astronomy, Inc., under NASA contract NAS 526555. Support for MAST for non-*HST* data is provided by the NASA Office of Space Science via grant NAG5-7584 and by other grants and contracts. This research includes data from the European Space Agency (ESA) mission *Gaia* (https://www.cosmos.esa.int/gaia), processed by the *Gaia* Data Processing and Analysis Consortium (DPAC, https://www.cosmos.esa.int/web/gaia/dpac/consortium). Funding for the DPAC has been provided by national institutions, in particular the institutions participating in the *Gaia* Multilateral Agreement. This research has made use of the SIMBAD database and the VizieR catalog access tool (doi:10.26093/cds/vizier), both operated at CDS, Strasbourg, France. The original description of the VizieR service was published in Ochsenbein et al. (2000), and the description for SIMBAD was published in Wenger et al. (2000). This research has made use of NASA's Astrophysics Data System Bibliographic Services.

Facilities: Gaia, *Kepler*.

Software: `astrobase` (Bhatti et al. 2017), `astropy` (Astropy Collaboration et al. 2018), `FITSH` (Pál 2012), `k2mosaic` (Barentsen 2016), `matplotlib` (Hunter 2007), `numpy` (Oliphant 2006), `scikit-learn` (Pedregosa et al. 2011), `scipy` (Jones et al. 2001), `VARTOOLS` (Hartman & Bakos 2016).

ORCID iDs

Joshua J. Wallace https://orcid.org/0000-0001-6135-3086
Joel D. Hartman https://orcid.org/0000-0001-8732-6166
Gáspár Á. Bakos https://orcid.org/0000-0001-7204-6727

References

Adams, F. C., Hollenbach, D., Laughlin, G., & Gorti, U. 2004, ApJ, 611, 360
Alard, C., & Lupton, R. H. 1998, ApJ, 503, 325
Armitage, P. J. 2000, A&A, 362, 968
Arzoumanian, Z., Joshi, K., Rasio, F. A., & Thorsett, S. E. 1996, in ASP Conf. Ser. 105, IAU Coll. 160, Pulsars: Problems and Progress, ed. S. Johnston, M. A. Walker, & M. Bailes (San Francisco, CA: ASP), 525
Astropy Collaboration, Price-Whelan, A. M., Sipőcz, B. M., et al. 2018, AJ, 156, 123
Backer, D. C., Foster, R. S., & Sallmen, S. 1993, Natur, 365, 817
Barentsen, G. 2016, barentsen/k2mosaic: v2.0.0, Zenodo, doi:10.5281/zenodo.167343
Beer, M. E., King, A. R., & Pringle, J. E. 2004, MNRAS, 355, 1244
Bhatti, W., Bouma, L. G., & Wallace, J. 2017, astrobase, Zenodo, doi:10.5281/zenodo.1011188
Bonnell, I. A., Smith, K. W., Davies, M. B., & Horne, K. 2001, MNRAS, 322, 859
Braga, V., Dall'Ora, M., Bono, G., et al. 2015, ApJ, 799, 165
Breslau, A., Steinhausen, M., Vincke, K., & Pfalzner, S. 2014, A&A, 565, A130
Chen, J., & Kipping, D. 2017, ApJ, 834, 17
Claret, A. 2018, A&A, 618, A20
Davies, M. B., & Sigurdsson, S. 2001, MNRAS, 324, 612
Ercolano, B., & Clarke, C. J. 2010, MNRAS, 402, 2735
Fischer, D. A., & Valenti, J. 2005, ApJ, 622, 1102
Ford, E. B., Joshi, K. J., Rasio, F. A., & Zbarsky, B. 2000, ApJ, 528, 336
Ford, E. B., Quinn, S. N., & Veras, D. 2008, ApJ, 678, 1407
Fregeau, J. M., Chatterjee, S., & Rasio, F. A. 2006, ApJ, 640, 1086
Fressin, F., Torres, G., Charbonneau, D., et al. 2013, ApJ, 766, 81
Gaia Collaboration, Brown, A. G. A., Vallenari, A., et al. 2016a, A&A, 595, A2
Gaia Collaboration, Brown, A. G. A., Vallenari, A., et al. 2018, A&A, 616, A1
Gaia Collaboration, Prusti, T., de Bruijne, J. H. J., et al. 2016b, A&A, 595, A1
Gilliland, R. L., Brown, T. M., Guhathakurta, P., et al. 2000, ApJL, 545, L47
Gratton, R. G., Carretta, E., & Bragaglia, A. 2012, A&ARv, 20, 50
Hamers, A. S., & Tremaine, S. 2017, AJ, 154, 272
Harris, W. E. 1996, AJ, 112, 1487
Hartman, J. D., & Bakos, G. Á. 2016, A&C, 17, 1
Hendricks, B., Stetson, P. B., VandenBerg, D. A., & Dall'Ora, M. 2012, AJ, 144, 25
Howard, A. W., Marcy, G. W., Bryson, S. T., et al. 2012, ApJS, 201, 15
Howell, S. B., Sobeck, C., Haas, M., et al. 2014, PASP, 126, 398
Hunter, J. D. 2007, CSE, 9, 90
Husser, T. O., Wende-von Berg, S., Dreizler, S., et al. 2013, A&A, 553, A6
Ida, S., & Lin, D. N. C. 2004, ApJ, 616, 567
Johansen, A., Youdin, A., & Mac Low, M.-M. 2009, ApJL, 704, L75
Johnson, J. A., Aller, K. M., Howard, A. W., & Crepp, J. R. 2010, PASP, 122, 905
Johnson, J. L., & Li, H. 2012, ApJ, 751, 81
Jones, E., Oliphant, T., Peterson, P., et al. 2001, SciPy: Open Source Scientific Tools for Python, Version 1.1.0, http://www.scipy.org/
Kaluzny, J., Thompson, I. B., Rozyczka, M., et al. 2013, AJ, 145, 43
Kipping, D. M. 2013, MNRAS, 434, L51
Kovács, G., Bakos, G., & Noyes, R. W. 2005, MNRAS, 356, 557

Kovács, G., Zucker, S., & Mazeh, T. 2002, A&A, 391, 369
Lindegren, L., Hernández, J., Bombrun, A., et al. 2018, A&A, 616, A2
Lomb, N. R. 1976, Ap&SS, 39, 447
Maíz Apellániz, J., & Weiler, M. 2018, A&A, 619, A180
Mandel, K., & Agol, E. 2002, ApJL, 580, L171
Marigo, P., Girardi, L., Bressan, A., et al. 2017, ApJ, 835, 77
Masuda, K., & Hotokezaka, K. 2019, ApJ, 883, 169
Masuda, K., & Winn, J. N. 2017, AJ, 153, 187
Mayor, M., Marmier, M., Lovis, C., et al. 2011, arXiv:1109.2497
McWilliam, A., & Bernstein, R. A. 2008, ApJ, 684, 326
Michel, F. C. 1994, ApJ, 432, 239
Mochejska, B. J., Kaluzny, J., Thompson, I., & Pych, W. 2002, AJ, 124, 1486
Nascimbeni, V., Bedin, L. R., Piotto, G., De Marchi, F., & Rich, R. M. 2012, A&A, 541, A144
Neeley, J., Marengo, M., Bono, G., et al. 2015, ApJ, 808, 11
Ochsenbein, F., Bauer, P., & Marcout, J. 2000, A&AS, 143, 23
Oliphant, T. 2006, A Guide to NumPy (Spanish Fork, UT: Trelgol Publishing), http://www.tramy.us/numpybook.pdf
Pál, A. 2012, MNRAS, 421, 1825
Pedregosa, F., Varoquaux, G., Gramfort, A., et al. 2011, J. Mach. Learn. Res., 12, 2825
Penev, K., Bouma, L. G., Winn, J. N., & Hartman, J. D. 2018, AJ, 155, 165
Petigura, E. A., Marcy, G. W., Winn, J. N., et al. 2018, AJ, 155, 89
Pont, F., Zucker, S., & Queloz, D. 2006, MNRAS, 373, 231
Rasio, F. A. 1994, ApJL, 427, L107
Richer, H. B., Ibata, R., Fahlman, G. G., & Huber, M. 2003, ApJL, 597, L45
Riello, M., De Angeli, F., Evans, D. W., et al. 2018, A&A, 616, A3
Santos, N. C., Israelian, G., & Mayor, M. 2001, A&A, 373, 1019
Scargle, J. D. 1982, ApJ, 263, 835
Sigurdsson, S. 1992, ApJL, 399, L95
Sigurdsson, S., Richer, H. B., Hansen, B. M., Stairs, I. H., & Thorsett, S. E. 2003, Sci, 301, 193
Soares-Furtado, M., Hartman, J. D., Bakos, G. Á., et al. 2017, PASP, 129, 044501
Spurzem, R., Giersz, M., Heggie, D. C., & Lin, D. N. C. 2009, ApJ, 697, 458
Thompson, T. A. 2013, MNRAS, 431, 63
Thorsett, S. E., Arzoumanian, Z., Camilo, F., & Lyne, A. G. 1999, ApJ, 523, 763
Thorsett, S. E., Arzoumanian, Z., & Taylor, J. H. 1993, ApJL, 412, L33
Vanderburg, A., & Johnson, J. A. 2014, PASP, 126, 948
Vanderburg, A., Latham, D. W., Buchhave, L. A., et al. 2016, ApJS, 222, 14
Wallace, J. J. 2018, RNAAS, 2, 213
Wallace, J. J., Hartman, J. D., Bakos, G. A., & Bhatti, W. 2019a, ApJS, 244, 12
Wallace, J. J., Hartman, J. D., Bakos, G. Á, & Bhatti, W. 2019b, Light Curves from a Search for Variable Stars in the Globular Cluster M4 with K2, DataSpace at Princeton Univ., http://arks.princeton.edu/ark:/88435/dsp01h415pd368
Weldrake, D. T. F., Sackett, P. D., & Bridges, T. J. 2008, ApJ, 674, 1117
Weldrake, D. T. F., Sackett, P. D., Bridges, T. J., & Freeman, K. C. 2005, ApJ, 620, 1043
Wenger, M., Ochsenbein, F., Egret, D., et al. 2000, A&AS, 143, 9
Wright, J. T., Marcy, G. W., Howard, A. W., et al. 2012, ApJ, 753, 160
Yi, S., Demarque, P., Kim, Y.-C., et al. 2001, ApJS, 136, 417
Zhou, G., Huang, C. X., Bakos, G. Á., et al. 2019, AJ, 158, 141